APPLIED GEOPHYSICS, Vol.17, No.4 (December 2020), P. 501−512, 9 Figures.
DOI:10.1007/s11770-020-0846-2

Investigation of image segmentation effect on the accuracy of reconstructed digital core models of coquina carbonate*

Wang Hai-Tao[1,2,3], Wang Li[4,5], Lai Fu-Qiang♦[1,2,3], and Zhang Jin-Yan[6]

Abstract: Digital core models reconstructed using X-ray tomography (X-CT) enable the quantitative characterization of the pore structure in three dimensions (3D) and the numerical simulation of petrophysics. When the X-CT images accurately reflect the micro structures of core samples, the greyscale threshold in the image segmentation determines the accuracy of digital cores and the simulated petrophysical properties. Therefore, it is vital to investigate the comparison parameter for determining the key greyscale threshold and the criterion to describe the accuracy of the segmentation. Representative coquina digital core models from X-CT are used in this work to study the impact of grayscale threshold on the porosity, pore percolation, connectivity and electrical resistivity of the pore scale model and these simulations are calculated by Minkowski functions, component labeling and finite element method, respectively, to quantify the pore structure and simulate electrical resistivity. Results showed that the simulated physical properties of the digital cores, varied with the gradual increase of the greyscale threshold. Among the four parameters related to the threshold, the porosity was most sensitive and chose as the comparison parameter to judge the accuracy of the greyscale threshold. The variations of the threshold change the micro pore structures, and then the electrical resistivity. When the porosity of the digital core model is close to the experimental porosity, the simulated porosity exponent matches the experimental porosity exponents well. The good agreement proved that the porosity is the critical comparison parameter to describe the accuracy of image segmentation. The criterion is that the porosity of the digital core after segmentation should be close to the experimental porosity.
Keyword: Porous media, X-CT, image segmentation, digital core, electrical resistivity simulation

Introduction

Digital core models distinguish grains, pores, and fluids in pore spaces, and are used as a basis for the analysis and simulation of the hydraulic and petrophysical properties of porous media (Iassonov et al., 2009; Blunt et al., 2013). X-ray computed tomography

*Manuscript received by the Editor August 24, 2019; revised manuscript received February 19, 2021.
1. School of Petroleum Engineering, Chongqing University of Science & Technology, Chongqing 401331, China.
2. National and Local Joint Engineering Research Center of Shale Gas Exploration and Development, Chongqing 401120, China.
3. Key Laboratory of Complex Oil and Gas Field Exploration and Development, Chongqing University of Science & Technology, Chongqing 401331, China.
4. The First Oil Production Plant of Changqing Oilfield, PetroChina Company Limited, Shanxi Yan'An 716000, China.
5. Logging Application Research Institute, CNPC Logging, Shanxi Xi' An 710000, China.
6. Well Logging Company, Shengli Oilfield Service Corporation, Sinopec, Shandong Dongying 257096, China.
♦Corresponding author: Lai Fu-Qiang (Email: laifq1982@163.com; 604987028@qq.com)

(X-CT) is a nondestructive technology that yields high-resolution images of the matrices, pore spaces, and fluid distribution within porous materials in three dimensions (3D). X-CT images measure the attenuation of X-rays after passing through specimens. The intensity of attenuation is quantified by grayscale data and relates to composition, density, and incident X-ray energy. On the basis of X-CT images, digital core models reconstructed in 3D and then further numerically simulated in terms of their hydraulic and petrophysical properties have been widely applied to petroleum exploration and soil and subsurface water flow investigation. Arns (2002) utilizes X-CT to scan four Fontainebleau sandstones with porosities of 8%, 13%, 15%, and 22% and then calculates the electrical and acoustic properties with brine water saturation equal to 100% by using the finite element method (FEM) (Arns et al., 2002; Knackstedt et al., 2007). Knackstedt et al. (2007) apply the pore morphology method introduced by Hilpert and Miller (2001) to simulate the fluid distribution during drainage and then calculate the electrical resistivity by using the FEM. Liu et al. (2009) consider a water film in calculating the resistivity of Fontainebleau sandstones. Arns et al. (2003) and Arns et al. (2004) investigate the permeability of pore scale models on the basis of the lattice Boltzmann method (Pan et al., 2004). Corbett et al. (2017) build carbonate pore scale models on the basis of X-CT images and interpret a positive correlation between the experimental porosity exponent and the permeability of the carbonate samples according to the quantitative characterization of the microscopic pore structure of the pore scale models. With the exploration and exploitation of tight sandstones, carbonates, shale, and gas hydrate sediments, pore structure and pore type gradually and obviously affect petrophysical properties (Blunt et al., 2013; Corbett et al., 2017; Liu et al., 2017; Yan et al., 2018a; Dong et al., 2019; Yan et al., 2019; Dong et al., 2020; Wu et al., 2020). X-CT imaging and digital core models also play important roles in investigating the micropore structures of unconventional reservoirs. Liu et al. (2017 and 2021) combine X-CT and scanning electronic microscopy (SEM) images to reconstruct tight sandstone digital core models, characterize the nm- to cm-scale pore structure of the Yanchang Formation in the Ordos Basin in China, and investigate the effects of minerals on electrical resistivity. Wang (2018 and 2020) investigates the effects of pore types and pore clusters on electrical resistivity and permeability and proposes a new electrical model on the basis of pore structure (Wang and Zhang, 2019). Yan et al. (2018b) and Dong et al. (2019 and 2020) respectively study the electrical resistivity of a low-contrast reservoir and gas hydrate sediments, on the basis of which new reservoir evaluation models are proposed. Wu et al. (2020) reconstruct digital core models on the basis of SEM images to investigate the effects of pore types, mineral types, and fluid types on the electrical resistivity and elastic properties of shale reservoirs. On the basis of X-CT images, the contact angle representing wettability (Blunt et al., 2013) and the surface area of the interface (Wildenschild and Sheppard, 2013) between different fluid phases have also been determined.

Iassonov et al. (2009) point out that the development of image segmentation technologies is lagging behind the improvement of X-CT technology in the imaging of porous media and then present a review of key image segmentation methods. Many researchers have realized that pore structure affects the petrophysical properties of unconventional reservoirs, such as carbonate, tight sandstone, shale, and gas hydrate (Blunt et al., 2013; Corbett et al., 2017; Liu et al., 2017; Wang, 2018; Yan et al., 2018b; Dong et al., 2019; Wu et al., 2020). On the premise of the X-CT resolution being suitable for characterizing microstructures, the grayscale threshold affects the pore structure and physical properties of reconstructed pore scale models by segmented X-CT images. To choose a reasonable grayscale threshold in image segmentation and thereby reach an acceptable digital core model for pore structure characterization and physical simulation, the current study extracted two representative volume (REV) samples with a size of 600 and a super REV sample with a size of 800 from the X-CT images of a coquina sample (Liu et al., 2009; Vik et al., 2013; Corbett et al., 2017). The effects of the grayscale threshold on the porosity, pore percolation, connectivity, and electrical current flow were investigated accordingly. Porosity and pore connectivity were calculated by Minkowski functions (Vogel and Roth, 2001; Vogel et al., 2010). The component labeling algorithm (Hoshen and Kopelman, 1976) was used to judge the percolation of the REV samples. The FEM (Garboczi, 1998) was adopted to calculate electrical resistivity. Archie's law (Archie, 1942) was considered in defining the porosity exponent. According to the relationships of these parameters with the grayscale thresholds, the parameter that was most sensitive to the image segmentation threshold was determined. The parameter was then taken for comparison to segment

super REV X-CT images of coquina and then reconstruct a binary pore scale model. The comparison of the simulated porosity exponent of the segmented coquina model with the experimental porosity exponent validated the feasibility of taking the parameter most sensitive to the grayscale threshold as a comparison parameter for image segmentation.

Materials and methodology

1. Coquina sample

The samples in this investigation are coquina samples from pre-salt carbonate reservoirs that are mainly of lacustrine origin; they are defined as concentrations of shells or shelly fragments deposited from the actions of some agent of transport (Câmara et al. 2014; Corbett et al. 2017). In this investigation, the coquina samples were from the outcrops of the Morro do Chaves Formation in the Sergipe–Alagoas Basin in Brazil. Core plugs were drilled from a block in the lab and then cleaned and dried to calculate the porosity. Thereafter, the laboratory measured porosities from the weight volume measurement, Hassler measurement with a confining pressure of 1, 000psi, and microscopy analysis, are 24.0%, 19.5%, and 22.0%, respectively (in Figure 1a).

The core plugs were saturated in brine of 50,000 ppm NaCl for five days at ambient temperature to reach the saturation equilibrium. Afterward, the core plugs were set in a core holder with a confining pressure of 1,000 psi in ambient temperature to measure the electrical resistivity. The resistivity was recorded when no obvious vibration occurred in 1–2 h. This resistivity was defined as the resistivity of the core plugs fully saturated by brine and was denoted as R_0. The resistivity of brine, R_w, and the length and cross-sectional area of each core plug were measured. Then, the formation factor, FF, and the porosity exponent, m, were calculated using Archie's first equation in Equation (1) (Archie, 1942). For each core plug, the electrical resistivity was measured twice, and the porosity exponents were equal to 3.0 and 2.78 (Figure 1b).

$$FF = \frac{\sigma_w}{\sigma_0} = \frac{R_0}{R_w} = \frac{1}{\phi^m}, \quad (1)$$

where FF is the formation factor representing the ratio of the resistivity of the porous media fully saturated by brine, R_0, to the resistivity of brine, R_w; σ_0 is the conductivity of the porous media with brine water in the pore space; σw is the conductivity of brine; ϕ is the porosity in fraction; and m is the porosity exponent.

X-CT imaging enables the characterization of the

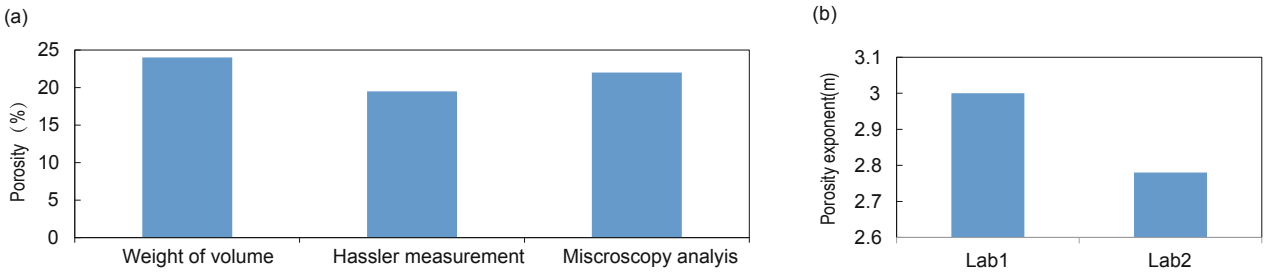

Fig. 1. Porosities and porosity exponents of coquina carbonates measured in the laboratory.

inner pores and mineral structures of core samples in 3D without destroying the samples. Therefore, the Skyscan 1173 high energy equipment was used to acquire the X-CT data, which included images measuring 1,368 × 1,368 and having a pixel size of 19.28 μm (Figure 2a) (Corbett et al., 2017). According to REV analysis (Liu et al., 2009), the size of a representative core sample is equal to 600 voxels (Wang, 2015; Corbett et al., 2017). In the current work, the core samples measuring 800 voxels were referred to as super REV samples (Figure 2b). The core samples measuring 600 voxels were called REV1 and REV2 (Figures 2c and 2d, respectively) and were used to investigate the effects of the grayscale threshold on the porosity, pore percolation, pore connectivity, and porosity exponent of the segmented pore scale models. The super REV samples were used to verify the image segmentation result on the basis of the effects of the grayscale threshold in segmentation on pore space and electrical resistivity.

2. Percolation of pore space

Microscopic pore structures affect the macroscopic properties of porous media (Blunt et al., 2013; Bultreys et al., 2016). The percolation of pore spaces in

segmented porous media is one of the most important parameters to describe the topology of micropore structures as it illustrates whether or not pore spaces are totally connected in one direction, as determined by searching and labeling the components in 3D binary images (Park and Rosenfeld, 1971). An important breakthrough in percolation determination is the introduction of multiple cluster labeling for 2D and 3D images known as the Hoshen–Kopelman algorithm (HKA) proposed by Hoshen and Kopelman (1976). This algorithm determines not only the percolation of a pore space in a specific direction but also the numbers and sizes of the components (clusters) in a single scan with consideration of diverse adjacencies. Adjacencies illustrate the connection of a voxel to its surrounding voxels known as neighbors in image processing. In 3D, the three types of adjacencies are 6, 18, and 26 adjacencies; that is, their voxels belong to their 6, 18, and 26 nearest neighbors, respectively. Meanwhile, 4 and 8 adjacencies are the only two types of connection for 2D. Herein, percolation was calculated by the HKA with 26 adjacencies.

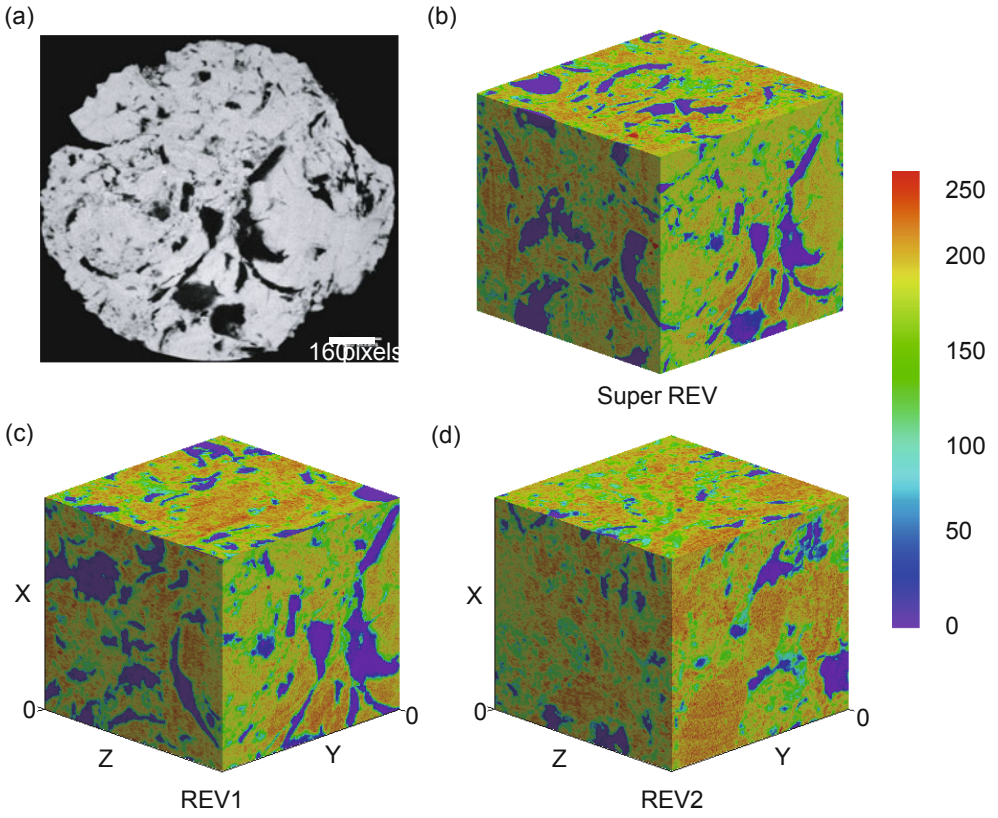

Fig. 2. X-ray CT slice of coquina: (a) a digital pore scale model of a super REV sample in 3D (800^3) based on the original X-CT data (b) and two REV samples (600^3), namely, REV1 (c) and REV2 (d), for investigating the effects of the image segmentation thresholds on the porosity, pore connectivity, pore percolation, and porosity exponent of the pore scale models.

3. Pore connectivity characterization

Minkowski functions are basic geometric measures defined for binary porous media after image segmentation (Vogel et al., 2010). For a binary porous medium, Ω, in d dimension with a pore space $X \subset \Omega$, a limited set of $d+1$ Minkowski functions is provided by its integral geometry. In 3D, four functions can be provided by Minkowski functions, as shown in Equation (2) (Vogel et al., 2010).

$$\begin{aligned} M_0(X) &= V_\Omega(X) \\ M_1(X) &= \int_{\delta X} ds = S(X) \\ M_2(X) &= \int_{\delta X} [\frac{1}{r_1} + \frac{1}{r_2}] ds = C(X), \\ M_3(X) &= \int_{\delta X} \frac{1}{r_1 r_2} ds = K(X) \end{aligned} \tag{2}$$

where δx represents the pore surface; ds is the surface element; and r_1 and r_2 are the minimum and maximum radii of curvature for the surface element, respectively.

The first function M_0 is the total mass of the structural unit corresponding to porosity, M_1 corresponds to surface density related to the interaction of solutes at pore–solid interfaces, the mean curvature M2 is correlated with the pore shape affecting the energy density of the wetting fluid or capillary pressure between different fluid phases, and M3 is related to the connectivity of the pores usually presented by a Euler number χ. The Euler number is defined by Equation (3) (Vogel et al., 2010).

$$\chi(X) = \mathrm{N} - \mathrm{L} + O = \frac{1}{4\pi} M_3(X), \tag{3}$$

where N is the number of isolated objects (closed convex); L is the number of redundant connections or loops (closed saddle surface); O is the number of cavities (closed concave); and M_3 is a dimensionless, topological measure that quantifies the connectivity of the pattern while M_0, M_1, and M_2 are metrics with units $[L_3]$, $[L_2]$, and $[L]$, respectively. Herein, the Euler number was divided by the volume of the samples to eliminate the effect of the volume of the samples on the number.

4. Electrical current simulation

The FEM is used to calculate the conductivity of reconstructed porous models in 3D on the basis of X-CT images after image segmentation. Garboczi (1998) develops an FEM algorithm and estimates the electrical properties of porous media. In this algorithm, a variational principle converts the solution of the Laplace equation into the optimization of system energy. The optimization is implemented by a fast conjugate–gradient method. In the current study, the FF was a conductivity (reciprocal of resistivity) ratio (Equation 1); hence, only the value of the conductivity of each phase in the segmented porous model in 3D was considered regardless of the unit. The porous model consisted of a matrix and a pore. The conductivity of the matrix grains was 0, while that of the pore, which was fully saturated by brine, was equal to 1. The FEM was used to calculate the current flow in the X, Y, and Z directions. The average of the currents of the porous model was the harmonic average of the electrical currents in three directions.

On the basis of the resistivity simulated by the FEM, the FF and porosity exponent were calculated by Archie's law (Archie, 1942) in Equation (1).

Results

1. Effects of grayscale threshold on segmented core samples

The grayscale threshold in image segmentation affects reconstructed digital core models and the petrophysical properties of corresponding digital core models. With the variation of the grayscale threshold in image segmentation, the changes in pore volume and the variations of pore percolation and connectivity affect the electrical current flow path and result in the vibration of electrical properties. When the grayscale threshold increases, the pore space gradually increases, and the porosity increases from 5% to 30% (Figure 3a). Herein, REV1 sequentially percolated in the Y, Z, and X directions when the grayscale threshold was equal to 20, 25, and 30, respectively (Figure 3b). The Euler number, which reflects pore connectivity (Figure 3c), dramatically increases to a peak of about 2.2 mm^{-3} when the grayscale threshold gradually reaches 20. This effect is due to the fact that the pore space percolates in neither direction and that the number of isolated pore clusters increases with an increase in the grayscale threshold. When the grayscale threshold further increases to 40, the pore space percolates in order in three directions, and the Euler number drops to 0.5 mm^{-3}. The number of isolated pore clusters and the number of connections increase with the further increase of the grayscale threshold. In such a case, the Euler number approaches 1.0 mm^{-3} until the grayscale threshold reaches 120. When the grayscale threshold exceeds 120, the isolated pore clusters further connect to one another, the number of isolated pore clusters decreases, the number of connections increases, and the Euler number drops.

With an increase in the grayscale threshold in this work, the pore space consecutively percolated in the Y, Z, and X directions, and the porosity exponent in each direction decreased (Figure 3d). With the percolation and increase of the pore space, the current density increased, hence the red color in Figure 4. Take the fourth column (Figures 4d, i, and n) as an example; from top to bottom, the color varied from −9 (Figure 4d) to −7.5 (Figure 4i) when the grayscale threshold ranged from 10 to 50. Meanwhile, the color varied from −7.5 (Figure 4i) to −7 (Figure 4n) when the grayscale threshold ranged from

50 to 90. With the variation of the current density, the porosity exponent began to converge (Figure 3d). When the grayscale threshold reached 60, the average porosity exponent slowly decreased from 3.0 to 2.5. When the grayscale threshold exceeded 70, the porosity exponent values mz, my, m, and mx consecutively decreased.

Therefore, when the grayscale threshold in the image segmentation reached a critical value, the pore space reached stability. Even with the further increase of the grayscale threshold, the pore connectivity and physical properties of the pore scale model remained almost stable, and the sensitivities of the properties to the grayscale threshold decreased.

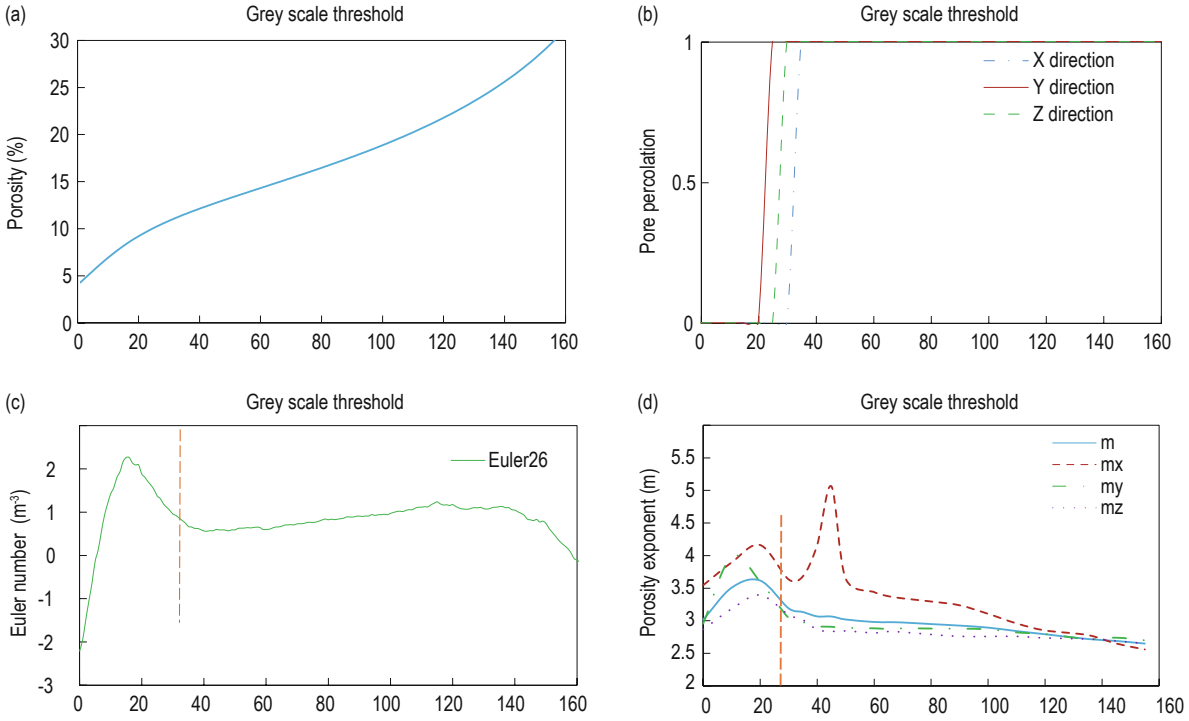

Fig. 3. Effects of image segmentation thresholds on the porosity (a), pore percolation (b), pore connectivity (c), and porosity exponent (d) of the pore scale model REV1 with various thresholds. The dotted lines in (c) and (d) reflect the percolation of the pore space in three directions.

The shape and distribution of the pore space (anisotropic and heterogeneous) result in the variation of the current density distributions in three directions. Figure 3 and Figure 4 clearly show that the variations of the pore shape and pore distribution caused differences in the electrical current density in three directions. The images in the same row in Figure 4 are equivalent to the same grayscale threshold. Owing to the variations of the pore space distribution in three directions, the electrical properties varied (Figures 4l, m, n and o). Take the third row as an example; the colors of the density distributions from X direction (Figure 4l), Y direction (Figure 4m), Z direction (Figure 4n) to average (Figure 4o) were almost the same, while the cross sectional areas of the pore space gradually reduced from XOY plane, XOZ plane to YOZ plane (Figure 4), and the porosity exponent increased from mz, my, and m to mx.

The properties of the segmented pore scale model were related to the grayscale threshold. Among these properties, only porosity showed a monotonic increase with the increase of the grayscale threshold. A monotonically increasing function is the simplest and the easiest relationship in these four correlations. Pore percolation and Euler number quantitatively characterize pore microstructures and thus affect the macroscopic physical properties of core samples (Blunt et al., 2013). Therefore, the alteration of pore connectivity and percolation with different grayscale thresholds explained the variation of the electrical porosity exponent of the REV samples in this work.

The comparison of Figures 3 and Figure 4 revealed that the correlations between the grayscale threshold and the porosity (Figure 5a and Figure 6a), pore percolation (Figure 5b and Figure 6b), pore connectivity (Figure 5c and Figure 6c), and electrical properties (Figure 5d and Figure 6d) of REV2 were almost the same as those of REV1. The porosity also monotonically increased with the increase of the grayscale threshold. Meanwhile, the Euler number began to drop when the grayscale threshold exceeded 140. However, the pore distribution,

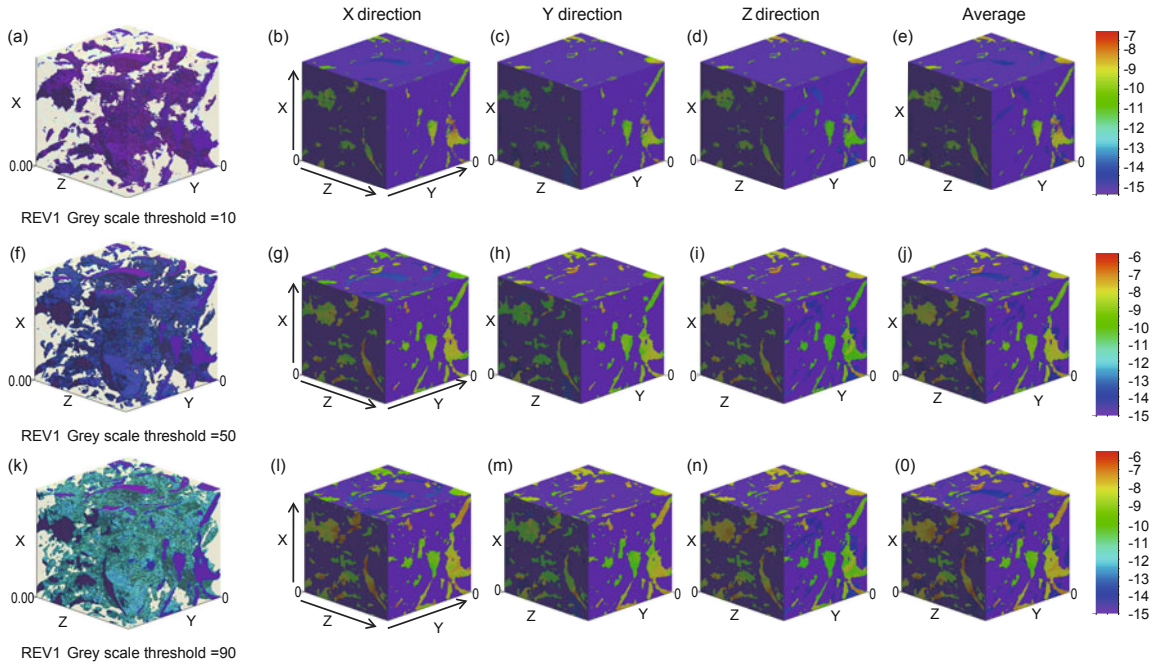

Fig. 4. Effects of image segmentation thresholds on electrical current density in the X, Y, and Z directions and the average electrical current density of the pore scale model REV1 with various thresholds. The legend is the logarithm of the current density.

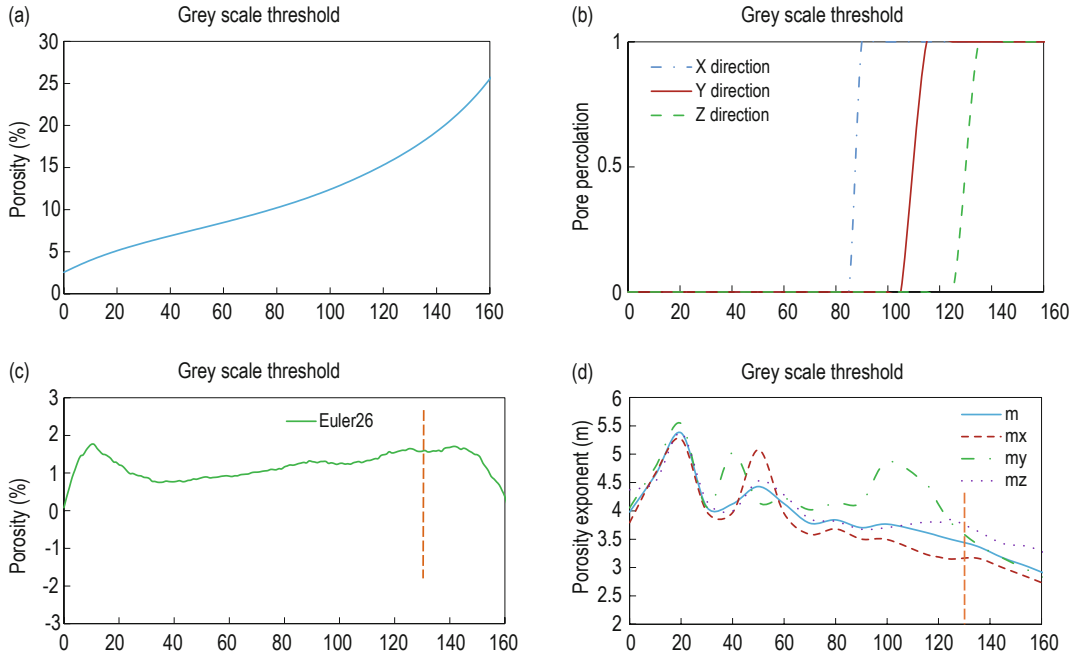

Fig. 5. Effects of the image segmentation thresholds on the porosity (a), pore percolation (b), pore connectivity (c), and porosity exponent (d) of the pore scale model REV2 with various thresholds.

pore percolation, and pore connectivity of REV2 were different from those of REV1. The pore space of REV2 consecutively percolated in the X, Y, and Z directions. When the pore space percolated in all three directions, the Euler number decreased to 0.2 mm^{-3}. Hence, the porosity exponent of REV2 gradually decreased from mx and my to mz. The variations of the pore space distribution in three directions caused the differences in the pore percolation, electrical current density distribution, and porosity exponents. For REV1 and REV2, the porosity, pore percolation, pore connectivity, and pore exponent varied, thereby reflecting the heterogeneity of the coquina sample.

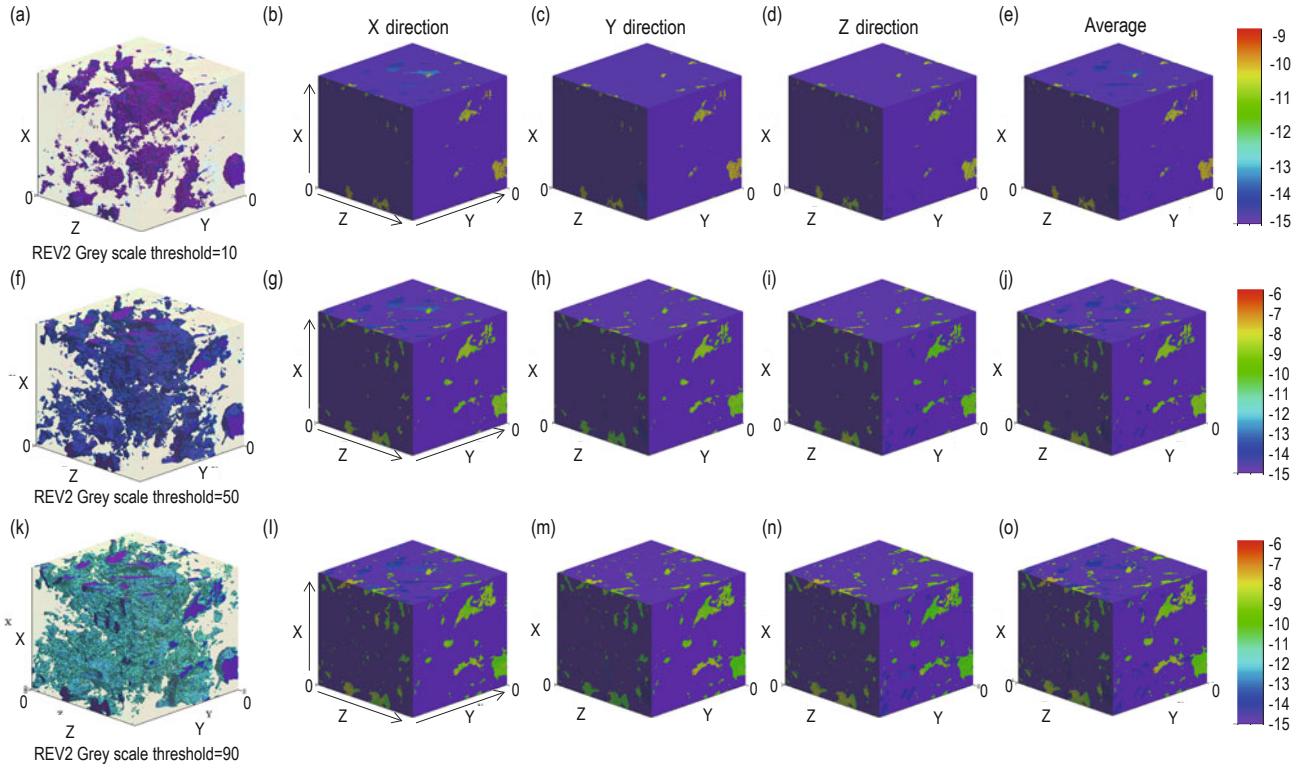

Fig. 6. Effects of the image segmentation thresholds on the electrical current density in the X, Y, and Z directions and the average electrical current density of the pore scale model REV2 with various grayscale thresholds. The legend is the logarithm of the current density.

2. Porosity as a comparison parameter in image segmentation

To quantitatively characterize the effects of the grayscale thresholds on porosity, pore percolation, pore connectivity, and porosity exponent, this study used the Morris screening method (Francos et al., 2003; Morris, 1991) in Equation (4). Specifically, such method was used to calculate the sensitivities of the aforementioned parameters to the grayscale thresholds in Figure 7.

$$S = \sum_{i=0}^{n-1} \frac{(Y_{i+1} - Y_i)/Y_0}{(P_{i+1} - P_i)/100} / (n-1), \quad (4)$$

where S is the sensitive factor, Y_i denotes the properties of the reconstructed pore scale model segmented by the ith grayscale threshold, Y_{i+1} denotes the properties of the reconstructed pore scale model segmented by the $i + 1$ th grayscale threshold, Y_0 denotes the properties of the pore scale model with a grayscale threshold equal to 0, Pi is the ith grayscale threshold, and n is the number of segmentations.

Sensitivity reduced from porosity, pore connectivity, and pore percolation to porosity exponent. Hence, porosity was found as the best comparison parameter to apply in image segmentation. Porosity was the most sensitive to the grayscale threshold (Figure 7) and was thus chosen as the comparison parameter to judge the accuracy of the grayscale threshold in image

segmentation. When the porosities of REV2 and REV1 were close to 20%, the pore spaces percolated in three directions, and the Euler numbers began to drop from 1.0 mm^{-3} to 0.0 mm^{-3} for REV1 (Figure 3) and from 1.5 mm^{-3} to 0.0 mm^{-3} for REV2 (Figure 5). Meanwhile, the average porosity exponent slowly decreased from 2.7 to 2.5 for REV1 (Figure 3) and rapidly decreased from 3.25 to 2.8 for REV2 (Figure 5). Therefore, porosity served as a comparison parameter to examine image segmentation, in which the porosity of the segmented pore scale model reconstructed by X-CT images should be close to the experimental porosity. According to this criterion, the coquina sample with a size of 800 (Figure 2b) and converted into the segmented binary pore scale model and the pore network extracted from the segmented pore scale model by the maximal ball method (Dong, 2007) are shown in Figure 8. In the figure, the red color denotes the pore body, and the blue color denotes the throat bond. With regard to the pore network for the coquina sample, the variations of the pore size and throat size were huge and indicated the abundance of isolated pore clusters existing in the pore space. Figure 9a lists the porosities of the binary pore scale model and various methods. Figure 9b compares the calculated porosity exponent of the binary segmented pore scale model by the global grayscale threshold with the two experimental porosity exponents. The porosity exponent matched the experimental data well, thereby validating the feasibility of taking porosity as the comparison parameter in image segmentation.

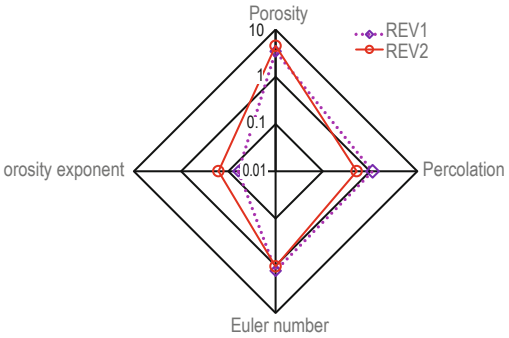

Fig. 7. Sensitivity of the porosity, pore percolation, pore connectivity (Euler number), and porosity exponent of the reconstructed pore scale model after segmentation to the grayscale thresholds of the segmentation.

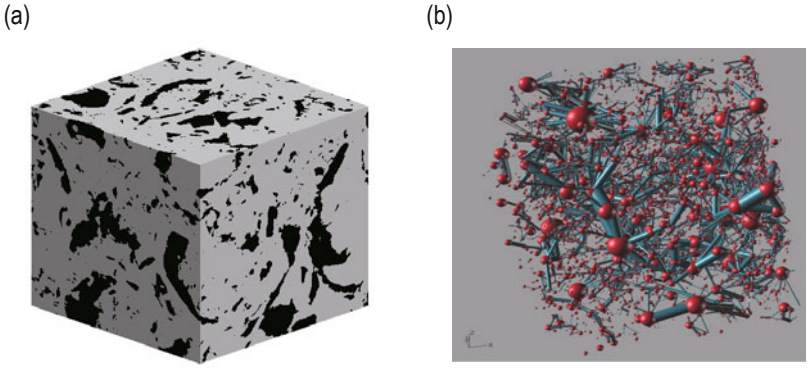

Fig. 8. Coquina binary core model (800^3) after image segmentation and the extracted pore network, with the red color denoting the pore nodes and the blue color denoting the throat bonds.

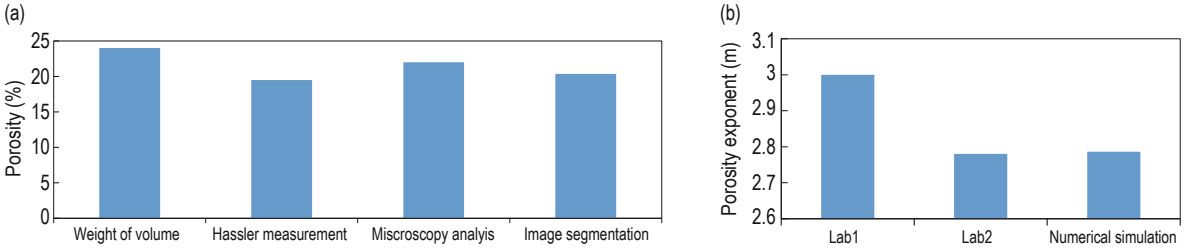

Fig. 9. Porosity and calculated porosity exponents of the segmented coquina model 8003 relative to the measured porosity and porosity exponent of the coquina sample in the laboratory.

Conclusions

This study investigated the effects of the grayscale threshold on the segmentation of X-CT images, which enable the accurate reflection of the microstructures of core samples. Specifically, a super representative coquina sample in 800^3 and two representative samples (600^3) were applied to investigate the effects of the grayscale threshold on the porosity, pore percolation, pore connectivity, and porosity exponent of the binary pore scale model after image segmentation by the grayscale threshold. The component labeling method, Minkowski functions, FEM, and Archie's law were used to determine pore percolation, pore connectivity, resistivity of porous media, and porosity exponent, respectively. The results indicated the following. (1) The relationships of the properties of the segmented pore scale models with the grayscale threshold varied, with the most sensitive parameter being porosity. (2) The microscopic pore structure determined the macroscopic properties of each core sample. Therefore, the micropore distribution and pore connectivity affected the electrical resistivity. (3) The complexity of the coquina carbonate pore space caused the heterogeneity and anisotropy of the petrophysics. (4) This study highlighted the effects of the grayscale threshold on porosity, pore percolation, pore connectivity, and porosity exponent. Moreover, observations indicated that the pore percolation, Euler number, and porosity exponent presented the same variations for REV1 and REV2 when the porosity was close to the experimental data. According to these findings, porosity as a comparison factor determined the accurate grayscale threshold in the segmentation of the X-CT images, with resolutions suitable for the characterization of microstructures. The determination criterion was as follows: the porosity of the digital core model after image segmentation should be close to the experimental porosity. With this criterion, the simulated porosity exponent of the super REV binary pore scale model after image segmentation matched the experimental data well. This result thus validated the feasibility of taking porosity as a comparison parameter in image segmentation.

Acknowledgment

We thank Patrick Corbett of Herriot–Watt University for providing the CT scans of the samples. The investigation is financially supported by the National Science & Technology Major Special Project (No. 2016ZX05006-002), China Postdoctoral Science Foundation Funded Project (No.2018M632716), Shandong Province Post Doctor Innovative Project Special Fund, Open Project Fund of the National and Local Joint Engineering Research Center of Shale Gas Exploration and Development (No. YiqKTKFGJDFLHGCYJZX444-201901), and Chongqing Basic Research and Frontier Exploration Project (No. cstc2018jcyjax0503).

References

Archie, G.E., 1942, The Electrical Resistivity Log as an Aid in Determining Some Reservoir Characteristics: Transactions of the AIME, **146**(54), 54–62.

Arns, C.H., 2002, The Influence of Morphology On Physical Properties of Reservoir Rocks: PhD Thesis, The University of New South Wales, Sydney, Australia.

Arns, C.H., Knackstedt, M.A., Pinczewski, W.V., and Garboczi, E.J., 2002, Computation of linear elastic properties from microtomographic images: Methodology and agreement between theory and experiment: Geophysics, **67**(5), 1396–1405.

Arns, J.-Y., Arns, C.H., Sheppard, A.P., et al., 2003, Relative permeability from tomographic images; effect of correlated heterogeneity: Journal of Petroleum Science and Engineering, **39**(3), 247–259.

Arns, J.-Y., Robins, V., Sheppard, A.P., et al., 2004, Effect of Network Topology on Relative Permeability: Transport in Porous Media, **55**(1), 21–46.

Blunt, M.J., Bijeljic, B., Dong, H., et al., 2013, Pore-scale imaging and modelling: Advances in Water Resources, 51(Supplement C), 197–216.

Bultreys, T., De Boever, W., and Cnudde, V., 2016, Imaging and image-based fluid transport modeling at the pore scale in geological materials: A practical introduction to the current state-of-the-art: Earth-Science Reviews, 155(Supplement C), 93–128.

Câmara, R., Corbett, P., Tavares, C., et al., 2014, Carbonate Coquina Reservoirs - New Insights for Petrophysical Reservoir Characterisation: 76th EAGE Conference and Exhibition, Expanded Abstracts, Amsterdam, Netherlands, Page:1–5.

Corbett, P.W.M., Wang, H., Câmara, R.N., et al., 2017, Using the porosity exponent (m) and pore-scale resistivity modelling to understand pore fabric types in

coquinas (Barremian-Aptian) of the Morro do Chaves Formation, NE Brazil: Marine and Petroleum Geology, **88**, 628–647.

Dong, H., 2007, Micro-CT imaging and pore network extraction: PhD thesis, the Department of Earth Science and Engineering, Imperial College London, London, UK.

Dong, H., Sun, J., Arif, M., et al., 2020, A novel hybrid method for gas hydrate filling modes identification via digital rock: Marine and Petroleum Geology, **115**, 104255.

Dong, H., Sun, J., Zhu, J., et al., 2019, Developing a new hydrate saturation calculation model for hydrate-bearing sediments: Fuel, **248**, 27–37.

Francos, A., Elorza, F.J., Bouraoui, F., et al., 2003, Sensitivity analysis of distributed environmental simulation models: understanding the model behaviour in hydrological studies at the catchment scale: Reliability Engineering & System Safety, **79**(2), 205–218.

Garboczi, E.J., 1998, Finite element and finite difference programs for computing the linear electric and elastic properties of digital images of random materials: Technical Report http://fire.nist.gov/bfrlpubs/build98/art147.html, Building and Fire Research Laboratory, National Institute of Standards and Technology, Gaithersburg, USA.

Hilpert, M., and Miller, C.T., 2001, Pore-morphology-based simulation of drainage in totally wetting porous media: Advances in Water Resources, **24**(3), 243–255.

Hoshen, J., and Kopelman, R., 1976, Percolation and cluster distribution. I. Cluster multiple labeling technique and critical concentration algorithm: Physical Review B, **14**(8), 3438–3445.

Iassonov, P., Gebrenegus, T., and Tuller, M., 2009, Segmentation of X-ray computed tomography images of porous materials: A crucial step for characterization and quantitative analysis of pore structures: Water Resources Research, **45**(9), 1–12.

Knackstedt, M.A., Arns, C.H., Sheppard, A.P., et al., 2007, Archie's exponents in complex lithologies derived from 3D digital core analysis: SPWLA 48th Annual Logging Symposium Transactions, Austin, Texas, USA.

Liu, X., Sun, J., and Wang, H., 2009, Numerical simulation of rock electrical properties based on digital cores: Applied Geophysics, **6**(1), 1–7.

Liu, X., Wang, J., Ge, L., et al., 2017, Pore-scale characterization of tight sandstone in Yanchang Formation Ordos Basin China using micro-CT and SEM imaging from nm- to cm-scale: Fuel, **209**, 254–264.

Liu, X., Yan, J., Zhang, X., et al., 2021, Numerical upscaling of multi-mineral digital rocks: Electrical conductivities of tight sandstones: Journal of Petroleum Science and Engineering, 201, 108530:1–12.

Morris, M.D., 1991, Factorial Sampling Plans for Preliminary Computational Experiments: Technometrics, **33**(2), 161–174.

Pan, C., Hilpert, M., and Miller, C.T., 2004, Lattice-Boltzmann simulation of two-phase flow in porous media: Water Resources Research, **40**(1), W015011–W0150114.

Park, C., and Rosenfeld, A., 1971, Connectivity and genus in three dimensions: Technical Report TR-156-05/71, Computer Science Center, Maryland University, College Park USA.

Vik, B., Bastesen, E., and Skauge, A., 2013, Evaluation of representative elementary volume for a vuggy carbonate rock—Part: Porosity, permeability, and dispersivity: Journal of Petroleum Science and Engineering, 112(Supplement C), 36–47.

Vogel, H.J., and Roth, K., 2001, Quantitative morphology and network representation of soil pore structure: Advances in Water Resources, **24**(3-4), 233–242.

Vogel, H.J., Weller, U., and Schlüter, S., 2010, Quantification of soil structure based on Minkowski functions: Computers & Geosciences, **36**(10), 1236–1245.

Wang, H., 2015, Numerical Simulation of Resistivity and Investigation of Porosity Exponent in Carbonates, Institute of Petroleum Engineering,School of Energy, Geoscience, Infracture and Society,Heriot-Watt University, Edinburgh, Scotland, UK.

Wang, H., 2018, Investigating the effects of pore types on the pore geometry, topology and electrical resistivity in fractured and vuggy samples using pore-scale models: Geosystem Engineering, **22**(5), 251-262.

Wang, H., 2020, Effects of pore clusters on the permeability, formation factor and porosity exponent of porous media: Geosystem Engineering, **23**(2), 73–85.

Wang, H., and Zhang, J., 2019, The effect of various lengths of pores and throats on the formation resistivity factor: Journal of Applied Geophysics, **162**, 35–46.

Wildenschild, D., and Sheppard, A.P., 2013, X-ray imaging and analysis techniques for quantifying pore-scale structure and processes in subsurface porous medium systems: Advances in Water Resources, **51**(Supplement C), 217–246.

Wu, Y., Lin, C., Yan, W., et al., 2020, Pore-scale simulations of electrical and elastic properties of shale samples based on multicomponent and multiscale digital rocks: Marine and Petroleum Geology, **117**, 104369:1–17.

Yan, W., Sun, J., Golsanami, N., et al., 2019, Evaluation of wettabilities and pores in tight oil reservoirs by a new experimental design: Fuel, **252**, 272–280.

Yan, W., Sun, J., Sun, Y., and Golsanami, N., 2018a, A robust NMR method to measure porosity of low porosity rocks: Microporous and Mesoporous Materials, **269**, 113–117.

Yan, W., Sun, J., Zhang, J., et al., 2018b, Studies of electrical properties of low-resistivity sandstones based on digital rock technology: Journal of Geophysics and Engineering, **15**(1), 153–163.

Wang Hai-Tao, Lecturer, graduated from Heriot–Watt University with a PhD in petroleum engineering. He is currently a lecturer in the School of Petroleum Engineering in Chongqing University of Science and Technology. His main interests are well logging data processing and interpretation, digital petrophysical simulation, and digital rock and borehole model reconstruction.